Bulgarian Chemical Communications, Volume 55, Issue 3 (pp. 196-213) 2023 *DOI: 10.34049/bcc.55.3.5559*

Synthesis, characterization, cytotoxicity, DFT calculations, and DNA interaction studies of new Schiff base metal (II) complexes

E. Abdalrazaq[1*], R. K. R. Al-Shemary[2], A. A. Q. Jbarah[1]

[1]*Al-Hussein Bin Talal University, Faculty of Science, Department of Chemistry, P.O. Box 20, Ma'an, Jordan*
[2]*Department of Chemistry, College of Education for Pure Sciences, Ibn -Al-Haitham, University of Baghdad, Iraq*

Received: March 13, 2023; Revised: July 18, 2023

SYNOPSIS

New Schiff base metal (II) complexes were synthesized and characterized. The cytotoxicity efficiency of the complexes was tested. Molecular docking analysis of the Schiff base ligands and of the Cu (II) complexes was reported. Optimized structures, electronic structures, and HOMO-LUMO gaps of the complexes were investigated using DFT calculations. The study included thermal analysis, fluorescence studies, and DNA-binding assays of the synthesized complexes.

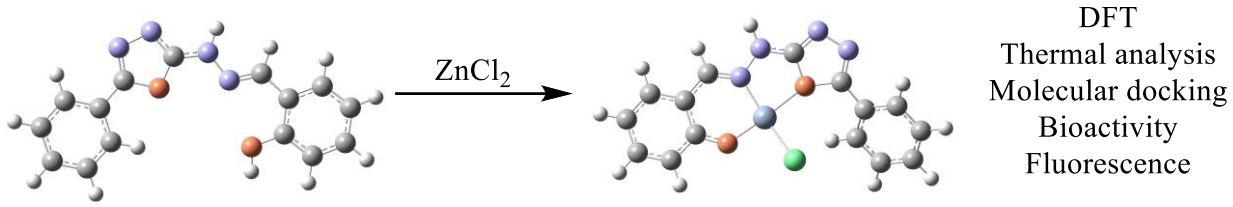

Mononuclear complexes of the type [M(L1-H)Cl], [M(L2-H)Cl], and [M(L3-H)Cl], where M = Ni^{2+}, Cu^{2+} or Zn^{2+}, L1 = (E)-2-((2-(5-phenyl-1,3,4-oxadiazol-2-yl) hydrazineylidene)methyl)phenolate, L2 = (E)-2-((2-(5-(4-hydroxyphenyl)-1,3,4-oxadiazol-2-yl) hydrazineylidene)methyl)phenolate and L3 = (E)-2-((2-(5-(4-chlorophenyl)-1,3,4-oxadiazol-2-yl) hydrazineylidene)methyl)phenolate, were synthesized and identified. The synthesized complexes were characterized by microelement analyses of metal content, Fourier transform infrared spectroscopy (FTIR), molar conductance, mass spectroscopy, magnetic measurements, thermal analysis, ^{13}C, and ^{1}H NMR, and UV–visible spectroscopy. Recorded FTIR data were supported by density functional theory (DFT) calculations. The vibrational frequencies of the molecules were computed using the optimized geometry obtained from the DFT calculations. According to the elemental analysis data and spectroscopic measurements tetrahedral structures were designated for all the complexes whilst Ni^{2+} complexes had a specified square planar structure. Cu^{2+} complex shows effective DNA cleavage in the non-attendance of factors of the exterior. Cu^{2+} complexes IC50 data explained the higher cytotoxicity efficiency compared to the other complexes. All the complexes react with CT–DNA by a groove system linking with DNA. Cytotoxicity efficacy was tested with cell lines of cancer like HCT–15, HeLa, and A549 where the Cu complex appears the most effective with HCT-15. Molecular docking analysis of Cu^{2+} complexes and ligands with human DNA topoisomerase was performed.

Keywords: Synthesis, DFT, cytotoxicity, studies of DNA interaction, Schiff base, complexes, molecular docking

INTRODUCTION

The studies of the coordination chemistry of biological ligands and their complexes significantly impact bioinorganic chemistry. Schiff bases are compounds that have many applications [1]. These compounds can be used in biological [2], photochemical [3], electrochemical [4], and catalytic activities [5].

The ligands and their metal complexes are also used as patterns to better understand biological modes [6]. The variable geometries of the Schiff base complexes make them substantial models of anthropomorphic chemical structures [7]. Transition metal complexes can cleave and link double-standard DNA [8], altering cancer cell expansion and DNA recurrence; this is the foundation for developing more effective anti-tumor

* To whom all correspondence should be sent:
E-mail: eidalzooby@yahoo.com

drugs [9, 10]. Understanding the different non-covalent DNA bonding patterns with these complexes [11], such as linking along outside the helix [12], linking along major or minor grooves [13, 14], planar aromatic ring intercalation, or forming planar molecules between pairs of bases, is critical for improving this type of anticancer drugs [15]. The flatness, chelation system [16], and type of donor atom in the ligands all play a role in calculating the complexes' intermediate ability to link with DNA [17]. Also, the secondary grooves are of interest for being free and able to carry enough room to link little molecules [18]. Most anticancer and antibiotic drugs are small molecules; hence, the major linking site is in the secondary DNA groove [19, 20].

In this study, we synthesized and characterized a chain of Zn(II), Cu(II), and Ni(II) complexes with Schiff base ligands. The efficacy of cytotoxicity was tested with cell lines of cancer like HCT–15, HeLa, and A549. Density functional theory (DFT) calculations, including geometry optimization, vibrational frequency analysis, and electronic structures, were reported for the synthesized molecules using B3LYP functional with the 6-31+G(d,p) basis set for C, H, O, N, and Cl atoms and the LANL2DZ basis set for metal atoms. In addition, molecular docking was performed for the ligands and complexes to investigate their interactions with the human DNA topoisomerase I (70 Kda) (PDB ID: 1SC7).

EXPERIMENTAL

Materials and physical measurements

All chemicals, reagents, and solvents used were of analytical grade and were used as received with no further purification. The materials were supplied by Sigma-Aldrich (St. Louis, MO, USA) and Merck (Darmstadt, Germany). ^{1}H and ^{13}C NMR spectra were recorded on 400 and 100 MHz Bruker NMR spectrometers, respectively. Elemental analysis (C, H, and N) was carried out using Thermoscientific Flash 2000. Infrared spectra were obtained with an Agilent Technologies Cary 630 FTIR spectrophotometer from 4000 to 600 cm^{-1} using the KBr disk method. Mass spectra were recorded on an LC Premier micro-mass spectrometer, and UV–Vis spectra were recorded on a Perkin-Elmer Lambda 25 UV–Vis spectrophotometer. The melting points of the ligands and complexes were measured by Stuart's SMP3 digital melting point apparatus using melting point capillary tubes. The molar conductivity measurements of the 10^{-3} mol L^{-1} complexes in dimethylformamide (DMF) were performed using a device of the digital conductivity series Ino.Lab.720. Magnetic measurements of the complexes were performed by using a Johnson Matthey balance. The fluorescence emission spectra were recorded using a Fluorolog-3, ISA (Jobin-Yvon-Spex, Edison, NJ, USA).

Synthesis of B1, B2 *and* B3

A 0.01 mol solution of benzoic acid (1.220 g), 4-hydroxybenzoic acid (1.381 g), or 4-chlorobenzoic acid (1.566 g) in 25 mL of ethanol was mixed with 5 mL of 98% H_2SO_4 and refluxed for 7 h. The solution was distilled under vacuum. The product was collected and washed with a solution of sodium carbonate (Scheme 1). A solution of 0.01 mol (0.50 mL) of 90% $NH_2NH_2{\cdot}H\text{-}H_2O$ in 50 ml of ethanol was added dropwise to the mixtures and refluxed with stirring for 5 h, then left to cool at room temperature. The solid products **B1**, **B2,** and **B3** were collected. The products were washed and recrystallized from the solvent (Scheme 1) [2, 3].

B1 compound: yellow solid; yield 76%; m.p. 158°C to 160°C; IR (ν_{max}, cm^{-1}):3342 cm^{-1} (v N-$H_{asym.}$), 3392 cm^{-1} (v N-H $_{sym.}$), 3294(v NH $_{amide}$), 1618(v C=O; EI-MS (m/z): 136.15 $[M]^+$; ^{1}H NMR(400 MHz, DMSO-d_6): δ 4.57 (d,2H, NH_2), 9.60 (s,1H, N-H), 7.48 to 8.00 (m,5H, aromatic protons), ^{13}C NMR (100 MHz, DMSO-d_6): δ176.86 (C=O), 126.65, 128.34, 130.78, 132.67, (aromatic carbons); Anal. % Found: C, 60.87; H, 5.43; N, 20.11; % Calcd.: C, 61.75;H, 5.92; N, 20.58%.

B2 compound: light yellow solid; yield 70%; m.p. 162°C to 164°C; IR (ν_{max}, cm^{-1}): 3421 cm^{-1} (v OH), 3338 cm^{-1} (v N-$H_{asym.}$), 3389 cm^{-1} (v N-H $_{sym.}$), 3290 (v NH $_{amide}$), 1616 (v C=O); EI-MS (m/z): 152.15 $[M]^+$; ^{1}H NMR(400 MHz, DMSO-d_6): δ 4.53 (d, 2H, NH_2), 9.64 (s, 1H, N-H), 7.43 to 8.01 (m,4H, aromatic protons), 9.69 (s, 1H, OH), ^{13}C NMR (100 MHz, DMSO-d_6): δ169.34 (C=O), 139.32 (COH), 121.32, 125.98, 129.76, (aromatic carbons); Anal. % Found: C, 56.34; H, 5.98; N, 19.17; %. Calcd.: C, 55.26; H, 5.30; N, 18.41%.

B3 compound: dark yellow solid; yield 88%; m.p. 167 °C to 169°C; IR (ν_{max}, cm^{-1}): 33427 cm^{-1} (v N-$H_{asym.}$), 3386 cm^{-1} (v N-H $_{sym.}$), 3288(v NH $_{amide}$), 1615 (v C=O), 830 (v C-Cl); EI-MS (m/z): 170.02 $[M]^+$; ^{1}H NMR (400 MHz, DMSO-d_6): δ 4.64 (d, 2H, NH_2), 9.54 (s, 1H, N-H), 7.40 to 8.12 (m,4H, aromatic protons);^{13}C NMR (100 MHz, DMSO-d_6): δ169.43 (C=O), 137.75 (C-Cl), 126.32, 126.78, 129.65,

(aromatic carbons); Anal. % Found: C, 49.82; H, 4.58; N, 16.68; %. Calcd.: C, 49.28; H, 4.14; N, 16.42%.

Synthesis of **E1**, **E2** *and* **E3**

A 0.01 mol solution of D1 (1.78 g), D2 (1.94 g), or D3 (2.13 g) and 0.01 mol (0.50 mL) of $NH_2NH_2.H_2O$ in 20 mL of absolute ethanol was refluxed for 7 hours. The products were filtered, washed, and dried under vacuum (Scheme 1).

E1 compound: brown solid; yield 77%; m.p. 210 °C to 212°C; IR (ν_{max}, cm^{-1}): 3423 cm^{-1} (v N-$H_{asym.}$), 3385 cm^{-1} (v N-$H_{sym.}$), 3084 (v CH $_{aromatic}$), 1663 (v C=N $_{endo.}$); EI-MS (m/z): 176.18 $[M]^+$; ^{1}H NMR (400 MHz, DMSO-d_6): δ 4.60 (d, 2H, NH_2), 8.90 (s, 1H, N-H), 6.97 to 7.82 (m, 5H, aromatic protons); ^{13}C NMR (100 MHz, DMSO-d_6): δ 173.12 (C=N), 125.98, 127.75, 129.54, 130.63 (aromatic carbons); Anal. %Found: C, 53.78; H, 4.21; N, 32.98; %Calcd.: C, 54.54; H, 4.58; N, 31.80.

E2 compound: dark brown solid; yield 75%; m.p. 208 °C to 211°C; IR (νmax, cm^{-1}): 3343 cm^{-1} (v OH.), 3475cm^{-1} (v N-$H_{asym.}$), 3380 cm^{-1} (v N-$H_{sym.}$), 3079 (v CH $_{aromatic}$), 1668 (v C=N $_{endo.}$); EI-MS (m/z): 192.18 $[M]^+$; ^{1}H NMR(400 MHz, DMSO-d_6): δ 4.60 (d, 2H, NH_2), 8.94 (s, 1H, N-H), 7.61 to 7.82(m,4H, aromatic protons), 9.58 (s,1H, OH);^{13}C NMR (100 MHz, DMSO-d_6): δ 167.43 (C=N), 125.54, 127.23, 129.87, 130.54, (aromatic carbons), 159.43 (COH); Anal. %Found: C, 50.65; H, 4.43; N, 29.87; %Calcd.: C, 50.00; H, 4.20; N, 29.15.

E3 compound: light brown solid; yield 70%; m.p. 200 °C to 202°C; IR (ν_{max}, cm^{-1}): 3423 cm^{-1} (v N-$H_{asym.}$), 3385 cm^{-1} (v N-$H_{sym.}$), 3084 (v $CH_{aromatic}$), 1663 (v C=N $_{endo.}$), 827 (v C-Cl); EI-MS (m/z): 210.03 $[M]^+$; ^{1}H NMR (400 MHz, DMSO-d_6): δ 4.62 (d, 2H, NH_2), 8.97 (s, 1H, N-H), 7.61 to 7.82 (m,4H, aromatic protons); ^{13}C NMR (100 MHz, DMSO-d_6): δ170.12 (C=N), 134.23 (C-Cl), 124.76, 128.82, 125.98, 130.32, (aromatic carbons); Anal. %Found: C,45.67; H, 2.47; N, 26.54; %Calcd. C, 45.45; H, 2.35; N, 26.60.

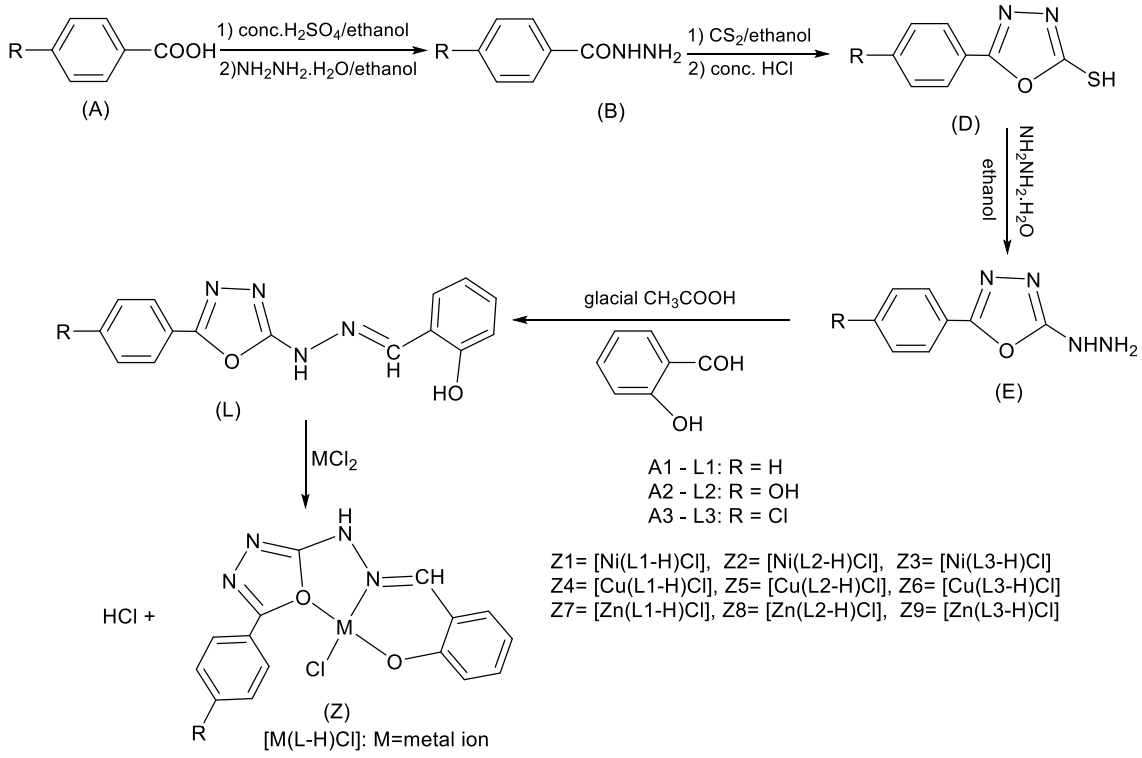

Scheme 1. Synthesis of L1-L3 Schiff bases and Z1-Z9 complexes

Preparation of Schiff base ligands **L1**, **L2,** *and* **L3**

A 0.001 mol solution (0.122 g) of 2-hydroxybenzaldehyde and some drops of glacial acetic acid were added to a 0.001 mol solution of E1 (0.176 g), E2 (0.192 g), or E3 (0.21 g) in 20 mL of absolute ethanol. The mixture was stirred and refluxed for 5 hours. The products were filtered, washed with ethanol, and dried under vacuum (Scheme 1).

L1 compound: green crystals; yield 80%; m.p. 129°C to 131 °C; IR (ν_{max}, cm^{-1}): 3325 cm^{-1} (v OH), 3320 (v NH $_{amide}$), 3150, 3087 (v CH $_{aromatic}$), 2931 (v CH $_{azomethine}$), 1678 (v C=N imine), 1625 (v C=N $_{oxadiazole}$ ring), 1262 (v(C-O) oxadiazole ring; EI-MS 280.29 (m/z): 280, 263, 187 111, 112, 94, 42; ^{1}H NMR (400 MHz, DMSO-d_6): 10.54 (s, 1H, N-H), 8.23 (s, 1H, HC=N), 6.78 to 8.30 (m, 9H, aromatic protons), 11.12 (s, 1H, OH); ^{13}C NMR (100 MHz, DMSO-d_6): δ 170. 9(C-O), 123.45, 124.56, 125.98, 130.98, (aromatic carbons), 144.54 (C=N), 159.21 (COH); Anal. %Found: C, 63.76; H, 4.65; N, 19.76; %Calcd.: C, 64.28; H, 4.32; N, 19.99.

L2 compound: light green crystals; yield 70%; m.p. 119°C to 121 °C; IR (ν_{max}, cm^{-1}): 3343, 3330 (v OH), 3313 (v NH $_{amide}$), 3158, 3090 (v CH $_{aromatic}$), 2937 (v CH $_{azomethine}$), 1674 (v C=N $_{imine}$), 1629 (v C=N $_{oxadiazole}$), 1268 (v(C-O) oxadiazole ring); EI-MS 296.29 (m/z): 296, 279, 203, 111, 112, 42; ^{1}H NMR(400 MHz, DMSO-d_6): 9.74 (s, 1H, OH), 10.52 (s,1H, N-H), 8.52 (s,1H, HC=N), 7.24 to 8.35 (m, 8H, aromatic protons),11.60 (s, 1H, OH); ^{13}C NMR (100 MHz, DMSO-d_6): δ 159.30 (OH), 170.67(C-O), 123.45, 124.76, 128.82, 125.98, 130.32 (aromatic carbons) 143.89 (C=N), 157.54 (COH); Anal. %Found: C, 60.56; H, 4.23; N, 18.78; %.Calcd.: C, 60.81; H, 4.08; N, 18.91.

L3 compound: yellowish green crystals; yield 77%; m.p. 112°C to 114 °C; IR (ν_{max}, cm^{-1}): 3347 cm^{-1} (v OH); 3319 (v NH amide), 3155, 3091 (v CH $_{aromatic}$), 2936 (v CH $_{azomethine}$), 1677 (v C=N $_{imine}$), 1629 (v C=N $_{oxadiazole}$), 1270 (v(C-O) oxadiazole ring), 830 (v C-Cl); EI-MS (m/z): 314, 232, 204, 187, 122, 112, 94, 70, 42; ^{1}H NMR (400 MHz, DMSO-d_6): 10.51 (s,1H, N-H), 8.45 (s,1H, HC=N), 7.30 to 8.32 (m, 8H, aromatic protons), 11.23 (s, 1H, OH); ^{13}C NMR (100 MHz, DMSO-d_6): δ 171.34(C-O), 124.0, 124.76, 128.82, 125.98, 130.32 (aromatic carbons), 134.23 (C-Cl) 144.12 (C=N), 156.98 (COH); Anal. %Found: C, 57.76; H, 11.34; N, 17.12; %.Calcd.: C, 57.24; H, 3.52; N, 17.80.

Synthesis of complexes

Z1 nickel (II) complex [Ni(L1-H)Cl]: brown solid; yield 74%; m.p. 179°C to 181°C; conductance (ΔM, Ω^{-1} cm^2 mol^{-1}; DMF) =19; μ_{eff} = 0.24 BM at 298 K; IR (ν_{max}, cm^{-1}): 3318 (v NH $_{amide}$), 3148, 3089 (v CH $_{aromatic}$), 2954 (v CH $_{azomethine}$), 1658 (v C=N $_{imine}$), 1620 (v C=N $_{oxadiazole}$), 1260 (v(C-O) oxadiazole ring), 465 (v Ni-N), 554 (v Ni-O) 431 (v Ni-Cl); EI-MS (m/z): 373.42, Anal. %Calcd. for $C_{15}H_{11}ClN_4NiO_2$: C, 48.25; H, 2.97; Cl, 9.49; N, 15.00; Ni, 15.72; % Found C, 46.26; H, 2.85; Cl, 9.10; N, 14.39; Ni, 15.07.

Z2 nickel (II) complex [Ni(L2-H)Cl]: brown solid; yield 67 %; m.p. 176°C to 179°C; conductance (ΔM, Ω^{-1} cm^2 mol^{-1}; DMF) = 24; μ_{eff} = 0.12 BM at 298 K; IR (ν_{max}, cm^{-1}): 3340 (v OH),3310 (v NH $_{amide}$), 3155, 3094 (v CH $_{aromatic}$), 2933 (v CH $_{azomethine}$), 1656 (v C=N $_{imine}$), 1625 (v C=N $_{oxadiazole\ ring}$), 1249 (v(C-O) oxadiazole ring), 445 (v Ni-N) 521(v Ni-O) 427 (v Ni-Cl); EI-MS (m/z): 389.42, Anal. %Calcd. for $C_{15}H_{11}ClN_4NiO_3$: C, 46.26; H, 2.85; Cl, 9.10; N, 14.39; Ni, 15.07; %Found: C, 46.65; H, 2.43; Cl, 9.08; N, 14.39; Ni, 15.32.

Z3 nickel (II) complex [Ni(L3-H)Cl]: greenish-brown; yield 82%; m.p. 165°C to 167°C; conductance (ΔM, Ω^{-1} cm^2 mol^{-1}; DMF) =18; μ_{eff} = 0.16 BM at 298 K; IR (ν_{max}, cm^{-1}): 3313 (v NH amide), 3150, 3089 (v CH $_{aromatic}$), 2933 (v CH $_{azomethine}$), 1660 (v C=N $_{imine}$), 1624 (v C=N oxadiazole ring), 1259 (v(C-O) oxadiazole ring), 843(v C-Cl), 456 (v Ni-N) 567 (v Ni-O) 421 (v Ni-Cl); EI-MS (m/z): 407.86, Anal. %Calcd. for $C_{15}H_{10}Cl_2N_4NiO_2$: C, 44.17; H, 2.47; Cl, 17.38; N, 13.74; Ni, 14.39; % Found: C, 43.87; H, 2.98; Cl,16.78; N, 13.87; Ni, 14.67.

Z4 copper(II) complex [Cu(L1-H)Cl]: reddish – brown solid; yield 79%; mp. 175°C to 177°C; Conductance (ΔM, Ω^{-1} cm^2 mol^{-1}; DMF) =20; μeff=1.76 BM at 298 K; IR (νmax, cm^{-1}): 3310 (v NH $_{amide}$), 3140, 3084 (v CH $_{aromatic}$), 2950 (v CH $_{azomethine}$), 1656 (v C=N $_{imine}$), 1621 (v C=N $_{oxadiazole}$ ring), 1261 (v(C-O) oxadiazole ring), 462 (v Cu-N), 550 (v Cu-O) 436 (v Cu-Cl); EI-MS (m/z): 378.28, Anal. %Calcd. for $C_{15}H_{11}ClCuN_4O_2$: C, 47.63; H, 2.93; Cl, 9.37; Cu, 16.80; N, 14.81; % Found: C, 47.43; H,2.11; Cl, 8.87; Cu, 16.43; N, 14.23.

Z5 copper(II) complex [Cu(L2-H)Cl]: brown solid; yield 76%; m.p. 170°C to 172°C; conductance (ΔM, Ω^{-1} cm^2 mol^{-1}; DMF) =17; μeff=1.79 BM at 298 K; IR (ν_{max}, cm^{-1}): 3337 (v OH), 3309 (v NH $_{amide}$), 3152, 3090 (v CH $_{aromatic}$), 2930 (v CH $_{azomethine}$), 1661 (v C=N $_{imine}$), 1622 (v C=N $_{oxadiazole}$ ring), 1255 (v(C-

O) oxadiazole ring), 543 (v Cu-O), 432 (v Cu-N), 412 (v Cu-Cl); EI-MS (m/z): 394.27, Anal. %Calcd. for $C_{15}H_{11}ClCuN_4O_3$ C, 45.70; H, 2.81; Cl, 8.99; Cu, 16.12; N, 14.21; %Found: C, 45.65; H, 2.43; Cl, 8.12; Cu, 15.76; N, 14. 09.

Z6 copper(II) complex [Cu(L3-H)Cl]: dark brown solid; yield 76%; m.p. 180°C to 182°C; UV-Vis (DMF, λ_{max}, nm (abs)): 367 (0.045), 279 (1.451), 783 (12,771); conductance (ΔM, Ω^{-1} cm^2 mol^{-1}; DMF) = 22; μeff =1.75 BM at 298 K; IR (ν_{max}, cm^{-1}): 3317 (v NH amide), 3145, 3089 (v CH $_{aromatic}$), 2943 (v CH azomethine), 1658 (v C=N $_{imine}$), 1620 (v C=N oxadiazole ring), 1250 (v(C-O) oxadiazole ring), 830 (v C-Cl), 563 (v Cu-O), 456 (v Cu-N), 412 (v Cu-Cl); EI-MS (m/z): 412.72, Anal. %Calcd. for $C_{15}H_{10}Cl_2CuN_4O_2$: C, 43.65; H, 2.44; Cl, 17.18; Cu, 15.40; N, 13.58; %Found: C, 43.11; H, 2.87; Cl, 17.54; Cu, 15.22; N, 13.89.

Z7 zinc(II) complex [Zn(L1-H)Cl]: brown solid; yield 68%; m.p. 179°C to 181°C; UV-Vis (DMF, λ_{max}, nm (Abs)): 367 (0.045), 279 (1.451), 275 (1.530); Conductance (ΔM, Ω^{-1} cm^2 mol^{-1}; DMF) = 21; IR (ν_{max}, cm^{-1}): 3314 (v NH $_{amide}$), 3144, 3082 (v CH $_{aromatic}$), 2956 (v CH $_{azomethine}$), 1657 (v C=N $_{imine}$), 1624 (v C=N $_{oxadiazole}$ ring), 1252 (v(C-O) oxadiazole ring), 466 (v Zn -N), 560 (v Zn -O) 438 (v Zn-Cl); EI-MS (m/z): 343.21; ^{1}H NMR(400 MHz, DMSO-d_6): 10.54 (s,1H, N-H), 7.65 (s,1H, HC=N), 6.78 to 8.30 (m,9H, aromatic protons),11.45 (s,1H, OH); ^{13}C NMR (100 MHz, DMSO-d_6): δ155.4 (C-N), 124.43, 124.58, 125.96, 130.93, (aromatic carbons), 144.54 (C=N); Anal. %Calcd. for $C_{15}H_{11}ClN_4O_2Zn$: C, 47.40; H, 2.92; Cl, 9.33; N, 8.42; Zn, 17.20; % Found: C, 47.54; H, 2.43; Cl, 9.78; N, 14.74, Zn, 17.87.

Z8 zinc(II) complex [Zn(L2-H)Cl]: brown solid; yield 68%; m.p. 175°C to 177°C; UV-Vis (DMF, λ_{max}, nm (Abs)): 367 (0.045), 279 (1.451), 275 (1.530); Conductance (ΔM, Ω^{-1} cm^2 mol^{-1}; DMF) = 23; IR cm^{-1}): 3335 (v OH), 3319 (v NH $_{amide}$), 3162, 3094 (v CH $_{aromatic}$), 2932 (v CH $_{azomethine}$), 1655 (v C=N $_{imine}$), 1621 (v C=N $_{oxadiazole}$ ring), 1251 (v(C-O) oxadiazole ring), 837 (v M-O), 567 (v Zn-O), 476 (v Zn-N), 432 (v Zn-Cl); EI-MS (m/z):396.11; ^{1}H NMR(400 MHz, DMSO-d_6): 9.74 (s, 1H, OH), 10.52 (s,1H, N-H), 7.70 (s,1H, HC=N), 7.24 to 8.35 (m, 8H, aromatic protons); ^{13}C NMR (100 MHz, DMSO-d_6): δ 159.30 (C-O), 156.8 (C-O), 123.46, 124.76, 128.84, 125.97, 130.34 (aromatic carbons) 143.89 (C=N), 157.54 (COH); Anal. %Calcd. for $C_{15}H_{11}ClN_4O_3Zn$: C, 45.48; H, 2z.80; Cl, 8.95; N, 14.14; Zn, 16.51. %Found: C, 45.78; H, 2.34; Cl, 8.12; N, 14.65; Zn, 16.22.

Z9 zinc (II) complex [Zn(L3-H)Cl]: brown solid; yield 68%; m.p. 185°C to 187°C; UV-Vis (DMF, λ_{max}, nm (Abs)): 367 (0.045), 279 (1.451), 275 (1.530); Conductance (ΔM, Ω^{-1} cm^2 mol^{-1}; DMF) = 25; IR (ν_{max}, cm^{-1}): 3318 (v NH amide), 3147, 3082 (v CH $_{aromatic}$), 2936 (v CH azomethine), 1659 (v C=N $_{imine}$), 1625 (v C=N oxadiazole ring), 1256 (v(C-O) oxadiazole ring), 840 (v C-Cl), 564 (v Zn-O), 467(v Zn-N), 422 (v Zn-Cl); ^{1}H NMR (400 MHz, DMSO-d_6): 10.51 (s,1H, N-H), 7.57 (s,1H, HC=N), 7.30 to 8.32 (m, 8H, aromatic protons); ^{13}C NMR (100 MHz, DMSO-d_6): δ 157.2 (C-O), 124.0, 124.76, 128.82, 125.98, 130.32 (aromatic carbons), 134.23 (C-Cl) 144.12 (C=N), 156.98 (COH); EI-MS (m/z): 414.55; Anal. %Calcd. for $C_{15}H_{10}Cl_2N_4O_2Zn$: C, 43.46; H, 2.43; Cl, 17.10; N, 13.52; O, 7.72; Zn, 15.77; %Found: C, 43.65; H, 2.43; Cl, 17.11; N, 13.67; Zn, 15.43.

DNA interaction studies

The studies of DNA cleavage and binding with complexes were carried out in Tris–HCl/NaCl buffer solutions [17].

Computational details

Gaussian 09 software [21] was used to perform the DFT calculations. All the structures of the compounds were optimized at the B3LYP level using the 6-31+G(d,p) basis set for C, H, O, N, and Cl atoms and the LANL2DZ basis set [22] for metal atoms. Several researchers used the LANL2DZ as a basis set in DFT calculations of systems that included metal atoms [23, 24]. GaussView 5.0, which is supported by Gaussian Inc. [21], was used to create the input files for the DFT calculations. The GaussView 5.0 software is used to visualize and analyze the data obtained from Gaussian09 output results. A frequency calculation was performed to identify the most stable structures of the synthesized compounds. The absence of the imaginary frequencies in the calculated vibrational modes indicates that the corresponding optimized structure of the molecule is the most stable one. The obtained values of the vibrational modes from the DFT calculations were scaled by a factor of 0.966 [25]. The energies and electron densities of the frontiers' molecular orbitals were calculated using the B3LYP level of theory and the LANL2DZ as a basis set. The excited states were computed for all compounds at the same level of theory using the TD-DFT (Time-Dependent Density Functional Theory) method [26]. The TD-DFT calculations were performed in DMSO solvent using the CPCM

solvation model (conductor-like polarizable continuum model) [27]. The projected density of states (PDOS) was obtained through the calculated orbital populations for all compounds at the same level of theory, using the GAUSSUM 3.0 program [28]. *lecular docking*

The structures of the ligands and their complexes were obtained by using DFT calculations using GaussView 5.0. A molecular docking study was done using topoisomerase I (70 kDa) (PDB ID: 1SC7) which was obtained from the RCSB protein data bank (http://www.rcsb.org/pdb). AutoDock Tool 4.2 [29] was used for the preparation of protein, grid, and missed atoms. The polar hydrogen atoms were added to the ISC7 receptor structure.

The Kollman charge was computed and added to the structures. A PDBQT file of protein structures was created by loading the receptor ISC7 into AutoDock Tool 4.2. A grid box with X: 60 Y: 60 Z: 60 Å, with a grid spacing of 0.5 Å, centered on X: 99.50. Y:1.82 Z: 11.35 Å was established to define the docking site on the protein. The Discovery Studio 4.0 client [30] was used to analyze the interactions of the compounds with ISC7.

RESULTS AND DISCUSSION

Synthesis of the compounds

Three types of ligands, L1, L2, and L3, have been synthesized in this work in four steps, beginning with a reaction of benzoic acid, 4-hydroxybenzoic acid, or 4-chlorobenzoic acid with an equimolar amount of $NH_2NH_2.H_2O$ and 98% H_2SO_4 (B products). In the second step, the reaction of the B product with CS_2 and KOH was in a 1:1 molar ratio. Third step: a solution of $NH_2NH_2.H_2O$ was mixed with a solution of the D product. Finally, equimolar amounts of 2-hydroxybenzaldehyde and E products from the previous step and some drops of glacial acetic acid were mixed to give L1, L2, and L3 ligands, according to Scheme 1, with a percentage yield of 80%, 70%, and 77%, respectively. The synthesized ligands are stable and soluble in THF, DMF, DMSO, dichloromethane, and chloroform. The complexes were prepared as shown in Scheme 1 by reaction of the ligand of $MCl_2.6H_2O$, or $ZnCl_2$, M is Ni or Cu, in a molar ratio of 1:1 (M:L) to give [M(L1-H)Cl], [M(L2-H)Cl], [M(L3-H)Cl] where M is Ni^{2+}, Cu^{2+}, or Zn^{2+}, with yields in the range of 67% - 82%. The obtained complexes are air-stable and soluble in DMSO, DMF, and dichloromethane. Mass spectrometry gave ion peaks M^+ at 373.42, 389.42, 407.86, 378.28, 394.27, 412.72, 343.21, 396.11, and 414.55 m/z, respectively, for Z1-Z9 complexes [14 .15]. The molecular masses correlate to the proposed structures and confirm the molar ratio of metal: ligand of 1:1 in all complexes.

FTIR spectral studies

Selected vibrational frequencies of the infrared spectra of the complexes (Z1-Z9) and the ligands (L1-L3) are given in Table S3. The assignments for the observed infrared bands were based on the calculated vibrational modes and the literature data [31-33]. The FTIR spectra of the ligands (L1-L3) show bands in the range 1678-1674 and 1270-1262 cm^{-1} are attributed to ν(C=N) imine and ν(C-O) oxadiazole, respectively. These modes were detected in the FTIR spectra of the complexes (Z1-Z9) in the ranges 1655-1662 cm^{-1} for ν(C=N) imines and 1249-1261 cm^{-1} for ν(C-O) oxadiazole. The chelation through the nitrogen atom of the imine group and the oxygen atom of the oxadiazole ring with the metal ion in complexes is supported by the downshifting of the vibrational frequencies of the (C=N) imine and (C-O) oxadiazole in the IR spectra of the complexes compared to those of the ligand [11]. In the FTIR spectra (Figures S1 and S2, see the ESI) of the ligands (L1-L3), a band appeared in the range of 3325-3347 cm^{-1} and was assigned to the stretching vibration of the hydroxyl group (ν(OH)) [12]. This band is absent in the FTIR spectra (Figures S3, S4, and S5) of the Z1, Z3, Z4, Z6, Z7, and Z9 complexes. This result is an indication of the coordination of the L1, L2, and L3 ligands *via* the oxygen atom of the hydroxyl group with the metal ion and the deprotonation of the hydroxyl group upon the complexation process. The ν(OH) appeared in the FTIR spectra (Figures S6, S7, and S8) of the Z2, Z5, and Z8 complexes, contrary to what was observed in the spectra of other complexes (Z1, Z3, Z4, Z6, Z7, and Z9). This result is due to the presence of two hydroxyl groups in the L2 ligand, which is coordinated with the metal ion via the oxygen atom of one hydroxyl group to form the Z2, Z5, and Z8 complexes. The coordination of the L1, L2, and L3 ligands *via* oxygen and nitrogen atoms is further supported by the observation of the bands in the ranges 476–432 and 521–567 cm^{-1} which are assigned to ν(M-N) and ν(M-O), respectively [13]. The above-mentioned observations are also concluded from the

calculated IR spectra for the ligands and complexes that are given in Table S3.

^{1}H NMR and ^{13}C NMR spectra

The ^{1}H NMR spectra (Figures S9, S10, and S11) of the ligands, L1, L2, and L3, show peaks as singlet signals for N-H, HC=N, OH, and C=NH groups at 10.51- 10.54, 8.23-8.52 ppm, 11.23-11.60 and 7.70–7.45 ppm, respectively [14]. Also in the spectra, peaks appeared at 6.78 to 8.32 ppm as multiplet signals and were assigned to aromatic protons. The ^{13}C NMR spectra (Figures S12 and S13) of the ligands showed peaks at 123.45–130.32 ppm and were assigned to aromatic carbon. The chemical shifts of the C signals of the C-O ring (155.4-157.2 ppm) in the zinc (II) complex spectra [15].

Mass spectral studies

The composition of the compound was characterized by mass spectra. The ligands L1, L2, and L3 showed peaks at m/z 280, 296, and 314, respectively. The molecular ions are confirmed by the peaks that appeared at m/z 378 (30%), 394 (25%), and 412 (70%). The observed molecular masses of the complexes were evidenced by ESI mass spectra peaks at m/z 378 (13%) and 412 (46%), coinciding with the molecular weights of complexes Z4 and Z6, respectively. They showed a base peak of L2 and L3 at 378 (80%) and 412 (90%) and identified the molecular weight of these ligands [16].

Geometry optimization of the complexes

Full geometry optimization of the Z1-Z9 complexes was performed using the DFT/B3LYP (exchange-correlation functional [34-36]) with the 6-31+G(d,p) basis set for C, H, O, N, and Cl atoms and the effective core potential LANL2DZ basis set for metal atoms. The optimized structures of the Z1, Z2, and Z3 (Ni^{2+}complexes) according to the B3LYP/LANL2DZ level of theory are displayed in Figure 1. The selected bond distances and angles of these complexes' optimized structures are listed in Table 1. The calculated geometries of Z1, Z2, and Z3 indicated a distorted square-planar environment around the central Ni atom. The result is obtained according to the calculated Cl-Ni-O and O-Ni-N angles of these complexes, which are close to 90° as listed in Table 1. The other features of Figure 1 that support the distorted square-planar environment around the central Ni atom are the calculated values of the Cl-Ni-N and O-Ni-O angles, which are close to 180°.

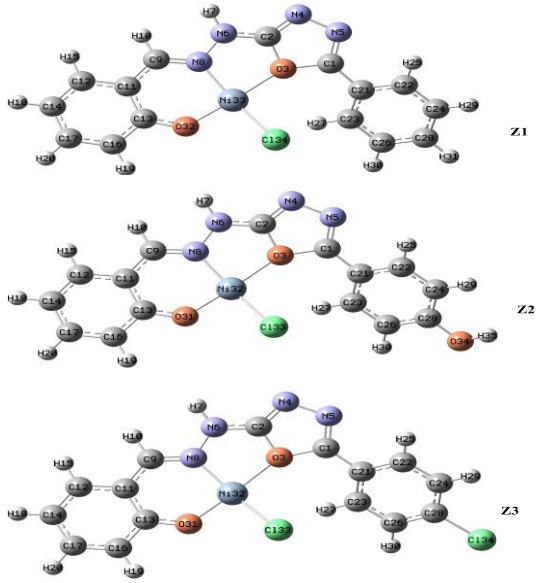

Figure 1. Optimized structures of Z1, Z2, and Z3 complexes according to DFT calculations using B3LYP functional with the 6-31+G(d,p) basis set for C, H, O, N, and Cl atoms and LANL2DZ basis set for the Ni atom.

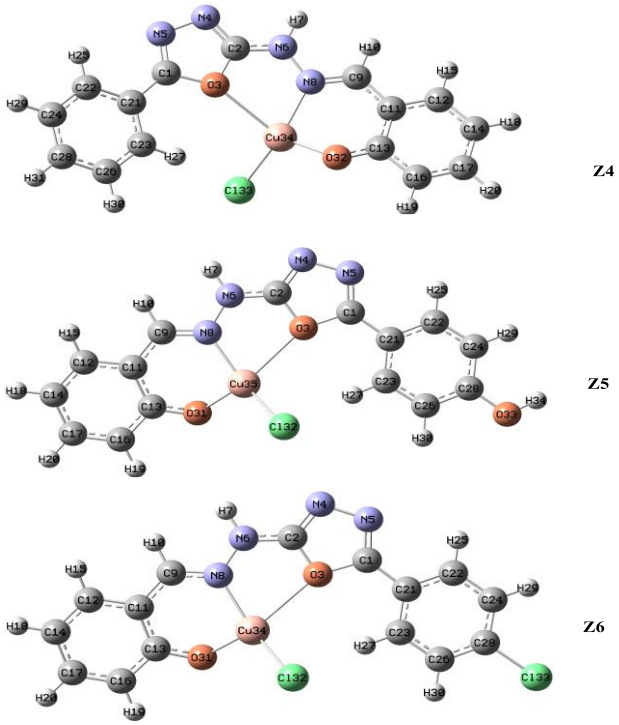

Figure 2. Optimized structures of Z4, Z5, and Z6 complexes according to DFT calculations using B3LYP functional with the 6-31+G(d,p) basis set for C, H, O, N, and Cl atoms and LANL2DZ basis set for the Cu atom.

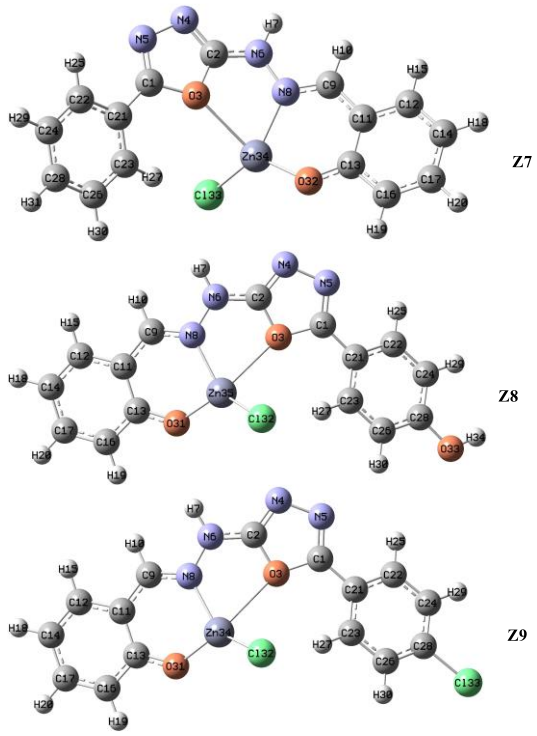

Figure 3. Optimized structures of Z7, Z8, and Z9 complexes according to DFT calculations using B3LYP functional with the 6-31+G(d,p) basis set for C, H, O, N, and Cl atoms and LANL2DZ basis set for the Zn atom.

The selected bond distances and angles of these complexes' optimized structures are listed in Table 2. The calculated geometries of Z4, Z5, and Z6 indicated a distorted tetrahedral environment around the central Cu atom. This conclusion is made from the calculated Cl-Cu-O and O-Cu-N angles of these complexes, which are listed in Table 2.

The optimized structures of Z7, Z8, and Z9 (Zn^{2+} complexes) according to the B3LYP/LANL2DZ level of theory are displayed in Figure 3. The selected bond distances and angles of these complexes' optimized structures are listed in Table 3. The calculated geometries of Z7, Z8, and Z9 indicated a distorted tetrahedral environment around the central Zn atom.

The optimized structures of Z7, Z8, and Z9 (Zn^{2+} complexes) according to the B3LYP/LANL2DZ level of theory are displayed in Figure 3. The selected bond distances and angles of these complexes' optimized structures are listed in Table 3. The calculated geometries of Z7, Z8, and Z9 indicated a distorted tetrahedral environment around the central Zn atom.

Table 1. Selected bond lengths (Å) and bond angles (°) of the computed structures of the Z1, Z2, and Z3 according to DFT calculations*.

Bond lengths (Å) of Z1		Bond lengths (Å) of Z2		Bond lengths (Å) of Z3	
Ni33-Cl34	2.210	Ni32-Cl33	2.211	Ni32-Cl33	2.211
O32-Ni33	1.823	O31-Ni32	1.823	O31-Ni32	1.821
N8-Ni33	1.922	N8-Ni32	1.922	N8-Ni32	1.921
O3-Ni33	2.067	O3-Ni32	2.068	O3-Ni32	2.074
N6-N8	1.404	N6-N8	1.404	N6-N8	1.404
N8-C9	1.321	N8-C9	1.321	N8-C9	1.321
Angles (°) of Z1		Angles (°) of Z2		Angles (°) of Z3	
Cl34-Ni33-O32	90.7	Cl33-Ni32-O31	90.6	Cl33-Ni32-O31	90.7
Cl34-Ni33-N8	168.9	Cl33-Ni32-N8	169.0	Cl33-Ni32-N8	168.7
Cl34-Ni33-O3	95.4	Cl33-Ni32-O3	95.4	Cl33-Ni32-O3	95.6
O32-Ni33-N8	93.5	O31-Ni32-N8	93.5	O31-Ni32-N8	93.5
O32-Ni33-O3	170.8	O31-Ni32-O3	170.8	O31-Ni32-O3	170.3
N8-Ni33-O3	81.8	N8-Ni32-O3	81.8	N8-Ni32-O3	81.8

*The DFT calculations are performed using B3LYP functional with the 6-31+G(d,p) basis set for C, H, O, N, and Cl atoms and LANL2DZ basis set for Ni atom.

Table 2. Selected bond lengths (Å) and bond angles (°) of the computed structures of the Z4, Z5, and Z6 according to DFT calculations*.

Bond lengths (Å) of Z4		Bond lengths (Å) of Z5		Bond lengths (Å) of Z6	
Cl33-Cu34	2.215	Cl32-Cu35	2.216	Cl32-Cu34	2.214
O32-Cu34	1.927	O31-Cu35	1.927	O31-Cu34	1.927
N8-Cu34	2.026	N8-Cu35	2.028	N8-Cu34	2.028
O3-Cu34	2.548	O3-Cu35	2.542	O3-Cu34	2.571
N8-C9	1.322	N8-C9	1.323	N8-C9	1.323
N6-N8	1.392	N6-N8	1.391	N6-N8	1.393
Angles (°) of Z4		Angles (°) of Z5		Angles (°) of Z6	
Cl33-Cu34-O32	108.3	Cl32-Cu35-O31	108.4	Cl32-Cu34-O31	108.7
Cl33-Cu34-N8	152.4	Cl32-Cu35-N8	152.3	Cl32-Cu34-N8	152.9
Cl33-Cu34-O3	100.8	Cl32-Cu35-O3	100.6	Cl32-Cu34-O3	99.9
O32-Cu34)-N8	90.4	O31-Cu35-N8	90.1	O31-Cu34-N8	90.2
O32-Cu34)-O3	141.7	O31-Cu35-O3	142.1	O31-Cu34-O3	142.5
N8-Cu34-O3	73.5	N8-Cu35-O3	73.6	N8-Cu34-O3	73.2

*The DFT calculations are performed using B3LYP functional with the 6-31+G(d,p) basis set for C, H, O, N, and Cl atoms and LANL2DZ basis set for Cu atom.

Table 3. Selected bond lengths (Å) and bond angles (°) of the computed structures of the Z7, Z8, and Z9 according to DFT calculations*.

Bond lengths (Å) of Z7		Bond lengths (Å) of Z8		Bond lengths (Å) of Z9	
Cl33-Zn34	2.252	Cl32-Zn35	2.252	Cl32-Zn34	2.249
O32-Zn34	1.920	O31-Zn35	1.920	O31-Zn34	1.916
N8-Zn34	2.069	N8-Zn35	2.068	N8-Zn34	2.065
O3-Zn34	2.559	O3-Zn35	2.569	O3-Zn34	2.652
N8-C9	1.328	N8-C9	1.328	N8-C9	1.330
N6-N8	1.406	N6-N8	1.406	N6-N8	1.407
Angles (°) of Z7		Angles (°) of Z8		Angles (°) of Z9	
Cl33-Zn34-O32	125.6	Cl32-Zn35-O31	125.7	Cl32-Zn34-O31	126.5
Cl33-Zn34-N8	135.5	Cl32-Zn35-N8	135.7	Cl32-Zn34-N8	136.5
Cl33-Zn34-O3	92.8	Cl32-Zn35-O3	92.3	Cl32-Zn34-O3	90.2
O32-Zn34-N8	90.5	O31-Zn35-N8	90.5	O31-Zn34-N8	91.0
O32-Zn34-O3	136.3	O31-Zn35-O3	136.4	O31-Zn34-O3	137.2
N8-Zn34-O3	70.5	N8-Zn35-O3	70.4	N8-Zn34-O3	69.3

*The DFT calculations were performed using B3LYP functional with the 6-31+G(d,p) basis set for C, H, O, N, and Cl atoms and LANL2DZ basis set for Zn atom.

UV-Vis results

The UV-Vis electronic absorption spectra (Figures S14–S21) of the ligands (L1-L3) and complexes (Z1-Z9) were experimentally recorded in the region of 200-1100 nm at ambient temperature in DMSO solvent with a concentration of 1 mM. Time-Dependent Density Functional Theory (TD-DFT [37-39]) calculations approach for the optimized geometry has been used to examine the electronic absorption behaviors of the studied compound in solvent media. In these calculations, we used B3LYP functional (exchange-correlation functional [34-36]) with the 6-31+G(d,p) basis set for C, H, O, N, and Cl atoms and the effective core potential LANL2DZ basis set for metal atoms.

The UV-vis spectra of the ligands show two absorption peaks. The first peaks for L1, L2, and L3 ligands appeared at 231, 225, and 231 nm, respectively, and were assigned to charge transfer transition (π→π*) [16]. The second peak appeared at 356, 350, and 363 nm for L1, L2, and L3 ligands, respectively, and is assigned to the charge transfer transition (n→π*) [16]. The UV-Vis spectra of the Z1, Z2, and Z3 complexes (Ni^{2+} complexes) show two bands. The bands that appeared at 465, 459, and 455 nm in the UV-Vis spectra of Z1, Z2, and Z3 complexes, respectively, are assigned to 2A1g → 2B1g transitions. The calculated value for this band is obtained at 471, 449, and 457 nm for Z1, Z2, and Z3, respectively, according to the TD-DFT results. The other band appeared at 645, 651, and 660 nm in the UV-Vis spectra of Z1, Z2, and Z3 complexes, respectively, and was assigned to 2A1g → 2A2g transitions. The calculated value of this band is observed at 655, 658, and 670 nm for Z1, Z2, and Z3, respectively. These results indicated a square planer environment around the central Ni atom, as evidenced by the calculated structures for these complexes (Figure 1).

The UV-Vis spectra of the Z4, Z5, and Z6 complexes (Cu^{2+} complexes) show a band in the range of 609–632 nm. The shape of this band is unsymmetrical, seeming to encompass several overlapping transitions. This band is similar to the reported absorption maximum for distorted tetrahedral Cu(II) complexes [40]. The TD-DFT calculation shows that these complexes (Z4, Z5, and Z6) exhibit two absorption bands that are very close to each other in the range of 600–640 nm. These two bands are separated by 15 to 18 nm. The result further supports that the Cu^{2+} complexes have two overlapped transitions in this range.

The UV-Vis spectra of the Z7, Z8, and Z9 complexes (Zn^{2+} complexes) exhibit two bands in the range of 374–280 and 465–490 nm. These bands are attributed to the C.T. transition. The absence of a band > 400 nm may be due to the MLCT of the d10 geometry of the zinc (II) ion [18]. The corresponding calculated UV-Vis spectra for the Z7, Z8, and Z9 complexes show three absorption bands for these complexes. The two bands are located very close to each other and in the range of 325–350 nm. The third band is observed in the range of 400–485 nm. A theoretical study of zinc(II) interactions with amino acid models and peptide fragments concluded that the zinc complexes prefer a tetrahedral geometry [41]. In our study, the calculated structures of the Z7, Z8, and Z9 complexes are found to have a distorted tetrahedral geometry.

The energy profiles of the HOMO, LUMO, and HOMO-LUMO gaps for Z4, Z5, and Z6 (Cu^{2+} complexes) are shown in Figure 5, using B3LYP functional with the 6-31+G(d,p) basis set for C, H, O, N, and Cl atoms and the LANL2DZ basis set for the Cu atom in DMSO solvent. Figure 5 shows the HOMO-LUMO energy gaps of Cu^{2+} complexes which are higher than those of Ni^{2+} complexes (Figure 4). The contribution of copper ions (Cu^{2+}) in the HOMO and LUMO orbitals in complexes Z4, Z5, and Z6 is very small (1-2%) which is contrary to nickel complexes (Figure 4). The imine group (N8=C9−H10) is the major contributor in the LUMO orbital of the Z4, Z5, and Z6 with 44, 46, and 42%, respectively. In the HOMO orbitals of the Z4, Z5, and Z6 The contributions of the imine group are 9, 7, and 9%, respectively. Also, the ortho-disubstituted benzene rings of the Z4, Z5, and Z6 notably contribute to the LUMO orbitals of these complexes with 31, 33, and 30%, respectively. A remarkable contribution of the disubstituted benzene rings of the Z4, Z5, and Z6 to the HOMO orbitals of these complexes is 39, 25, and 36%, respectively. The contribution of the oxadiazole ring is also 15, 20, and 17% to the HOMO orbitals of Z4, Z5, and Z6, respectively. While in the LUMO orbitals the contribution of the oxadiazole rings of Z4, Z5, and Z6, are 14, 12, and 15%, respectively.

Figure 6 shows the energy profile of the HOMO's, LUMO's, and HOMO-LUM-O gaps for the Zn^{2+} complexes Z7, Z8, and Z9, which are calculated at the B3LYP function with the 6-31+G(d,p) basis set for C, H, O, N, and Cl atoms and LANL2DZ basis set for zinc atom in DMSO solvent. The energy gaps of HOMO-LUMO in zinc complexes are higher than that of nickel complexes (Figure 4) and very close to copper complexes (Figure 5). In the HOMO and LUMO orbitals, the contribution of the zinc metal ion in the complexes Z7, Z8, and Z9 is very small (0–1%) as observed in the case of Cu^{2+} complexes. A remarkable contribution in the LUMO orbitals of the Z7, Z8, and Z9 is observed for the imine group (N8=C9−H10) with 42, 45, and 37%, respectively. The contribution of the imine group in the HUMO orbital is only 8% in the case of Zn^{2+} complexes. Also, the ortho-disubstituted benzene rings of the Z7, Z8, and Z9 notably contribute to the LUMO orbitals of these complexes with 29, 32, and 26%, respectively.

The major contributions of the HOMO orbitals of the Z7, Z8, and Z9 are observed for the disubstituted benzene ring at 48, 41, and 50%, respectively. The oxadiazole ring also contributed 15, 12, and 18% to the LUMO orbitals of Z7, Z8, and Z9, respectively. It was observed that the contribution of the oxadiazole ring in the HOMO orbitals of Z7, Z8, and Z9, is 10, 13, and 9%, respectively.

Electronic structures

The calculated energies and electron densities of the frontier's molecular orbitals were used to confirm the electronic properties of the complexes.

The energy profiles of the highest occupied molecular orbitals, HOMOs, lowest unoccupied molecular orbitals, LUMOs, and HOMO-LUMO gaps for Z1, Z2, and Z3 (Ni^{2+} complexes) are shown in Figure 4. The B3LYP functional with the 6-31+G(d,p) basis set is used to calculate the energies for C, H, O, N, and Cl atoms and the LANL2DZ basis set for Ni atoms using DMSO solvent. The Z1 complex explores the higher HOMO-LUMO energy gap. In complexes Z1, Z2, and Z3, the percent composition of the selected frontier-occupied and the virtual molecular orbitals are obtained based on the results of the projected density of states (PDOS) calculations.

The LUMO orbitals in the complexes Z1, Z2, And Z3 are mostly localized on Ni^{2+} ions in order of 66, 66, and 65%, respectively. Figure 4 does not show the contribution of the phenyl ring, phenol group, and chlorobenzene in Z1, Z2, and Z3 in the HOMO and LUMO orbitals.

The contribution of the imine group (N8=C9-H10) in HOMO and LUMO orbitals of the complexes Z1, Z2, and Z3 is only 7%. The HOMO orbital of these complexes (Z1, Z2, and Z3) is mostly localized on the ortho-disubstituted benzene ring with 48, 42, and 49%, respectively. The contribution of oxygen atoms to the HOMO orbitals in Z1, Z2, and Z3 complexes are 20, 17, and 20%, respectively.

The energy profiles of the HOMOs, LUMOs, and HOMO-LUMO gaps for Z4, Z5, and Z6 (Cu^{2+} complexes) are shown in Figure 5, using B3LYP functional with the 6-31+G(d,p) basis set for C, H, O, N, and Cl atoms and the LANL2DZ basis set for the Cu atom in DMSO solvent. Figure 5 shows the HOMO-LUMO energy gaps of Cu^{2+} complexes which are higher than that of Ni^{2+} complexes (Figure 4). The contribution of copper ions (Cu^{2+}) in the HOMO and LUMO orbitals in complexes Z4, Z5, and Z6 is very small (1-2%) which is contrary to nickel complexes (Figure 4). The imine group (N8=C9−H10) is the major contributor in the LUMO orbital of the Z4, Z5, and Z6 with 44, 46, and 42%, respectively. In the HOMO orbitals of the Z4, Z5, and Z6 The contributions of the imine group are 9, 7, and 9%, respectively. Also, the ortho-disubstituted benzene rings of the Z4, Z5, and Z6 notably contribute to the LUMO orbitals of these complexes with 31, 33, and 30%, respectively. A remarkable contribution of the disubstituted benzene rings of the Z4, Z5, and Z6 to the HOMO orbitals of these complexes is 39, 25, and 36%, respectively. The contribution of the oxadiazole ring is also 15, 20, and 17% to the HOMO orbitals of Z4, Z5, and Z6, respectively. While in the LUMO orbitals the contribution of the oxadiazole rings of Z4, Z5, and Z6, are 14, 12, and 15%, respectively.

Figure 6 shows the energy profile of the HOMO's, LUMO's, and HOMO-LUMO gaps for the Zn^{2+} complexes Z7, Z8, and Z9, which are calculated at the B3LYP function with the 6-31+G(d,p) basis set for C, H, O, N, and Cl atoms and LANL2DZ basis set for zinc atom in DMSO solvent. The energy gaps of HOMO-LUMO in zinc complexes are higher than that of nickel complexes (Figure 4) and very close to copper complexes (Figure 5). In the HOMO and LUMO orbitals, the contribution of the zinc metal ion in the complexes Z7, Z8, and Z9 is very small (0–1%) as observed in the case of Cu^{2+} complexes. A remarkable contribution in the LUMO orbitals of the Z7, Z8, and Z9 is observed for the imine group (N8=C9−H10) with 42, 45, and 37%, respectively. The contribution of the imine group in the HUMO orbital is only 8% in the case of Zn^{2+} complexes. Also, the ortho-disubstituted benzene rings of the Z7, Z8, and Z9 notably contribute to the LUMO orbitals of these complexes with 29, 32, and 26%, respectively. The major contributions of the HOMO orbitals of the Z7, Z8, and Z9 are observed for the disubstituted benzene ring at 48, 41, and 50%, respectively. The oxadiazole ring also contributed 15, 12, and 18% to the LUMO orbitals of Z7, Z8, and Z9, respectively. It was observed that the contribution of the oxadiazole ring in the HOMO orbitals of Z7, Z8, and Z9, is 10, 13, and 9%, respectively.

Measurement of molar conductivity

The measurements of molar conductivity (ΔM) for the Z1–Z9) complexes of mononuclear metal (II) were performed in DMF solvent, according to the conductance data (17–25 Ω^{-1} cm^2 mol^{-1}) of the

complexes, which is the non-electrolytic behavior of these complexes [19].

Magnetic properties

The corrected magnetic moments of metal (II) complexes (Z1–Z9) were measured and calculated using Pascal's constants. The magnitudes of the magnetic moments (1.75–1.79 BM) for Cu(II) complexes (Z4–Z6) are assigned to the spin only of the d^9 environment with one unpaired electron, confirming the tetrahedral environment around Cu(II) metal ions complexes. The magnetic moments of Ni(II) complexes (Z1-Z3) are in the 0.12 – 0.24 BM range and are attributed to a square planar environment, which agrees with the electronic transitions in the UV-vis spectra [20]. The Zn(II) complexes, (Z7–Z9), exhibit diamagnetic properties which are attributed to the d10 environment, as predictable. The electronic transitions in UV-Vis, magnetic susceptibility, and sensitivity values confirm a distorted tetrahedral environment for Zn(II) complexes (Z7-Z9) and Cu(II) complexes (Z4-Z6), and a distorted square planar environment for Ni^{2+} complexes (Z1-Z3).

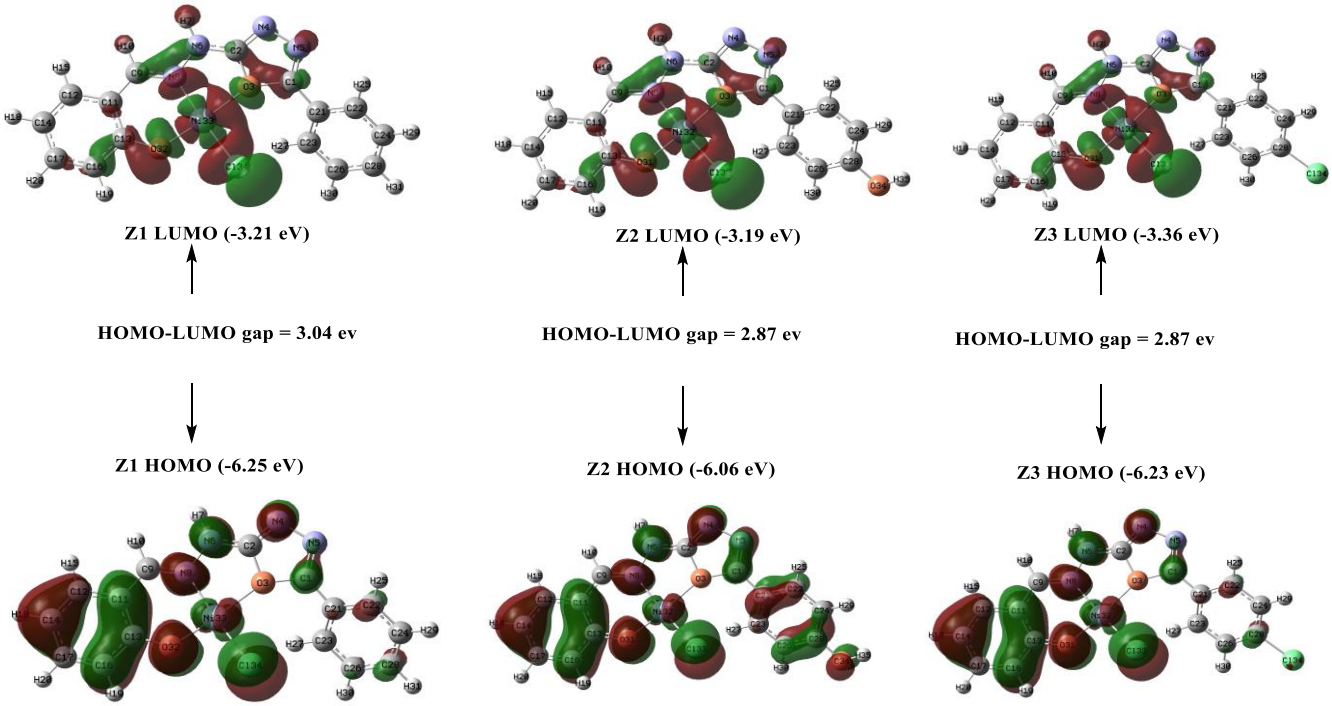

Figure 4. Energy profile of the frontier orbitals HOMO and LUMO, and HOMO-LUMO gaps for Z1, Z2, and Z3, calculated at the B3LYP functional with the 6-31+G(d,p) basis set for C, H, O, N, and Cl atoms and LANL2DZ basis set for Ni atom in DMSO as solvent.

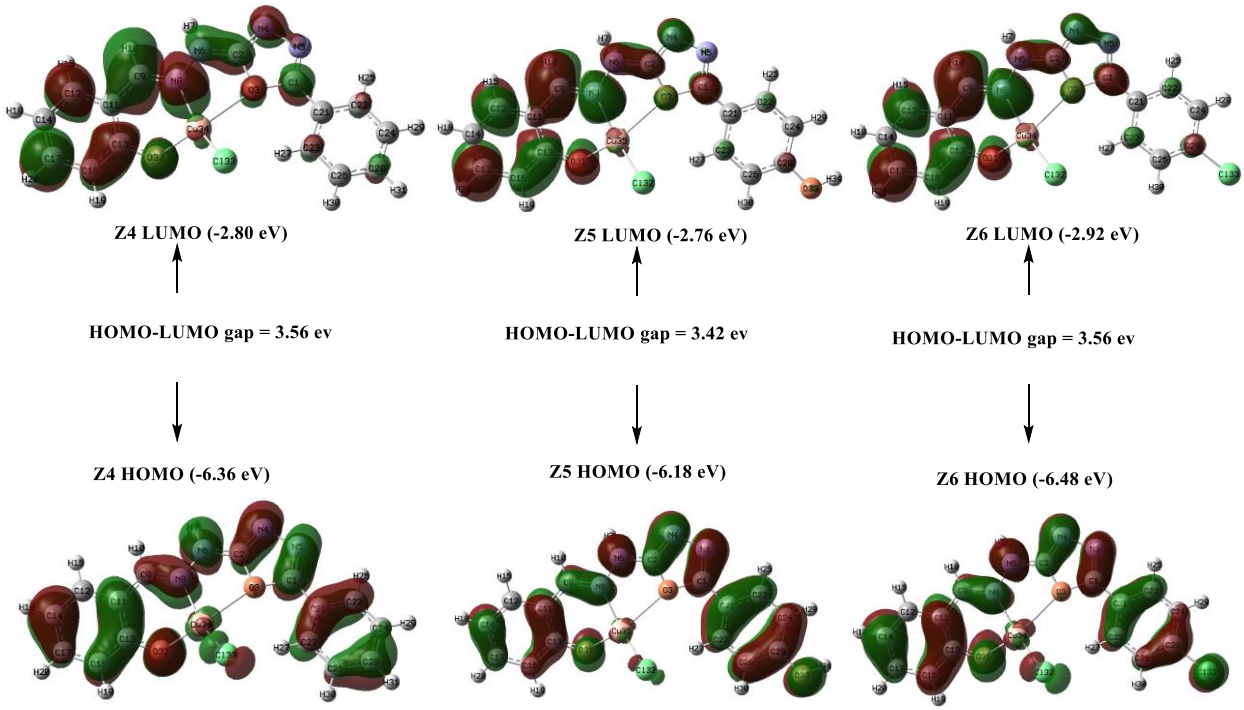

Figure 5. Energy profile of the frontier orbitals HOMO and LUMO, and HOMO-LUMO gaps for Z4, Z5, and Z6, calculated at the B3LYP functional with the 6-31+G(d,p) basis set for C, H, O, N, and Cl atoms and LANL2DZ basis set for Cu atom in DMSO as solvent.

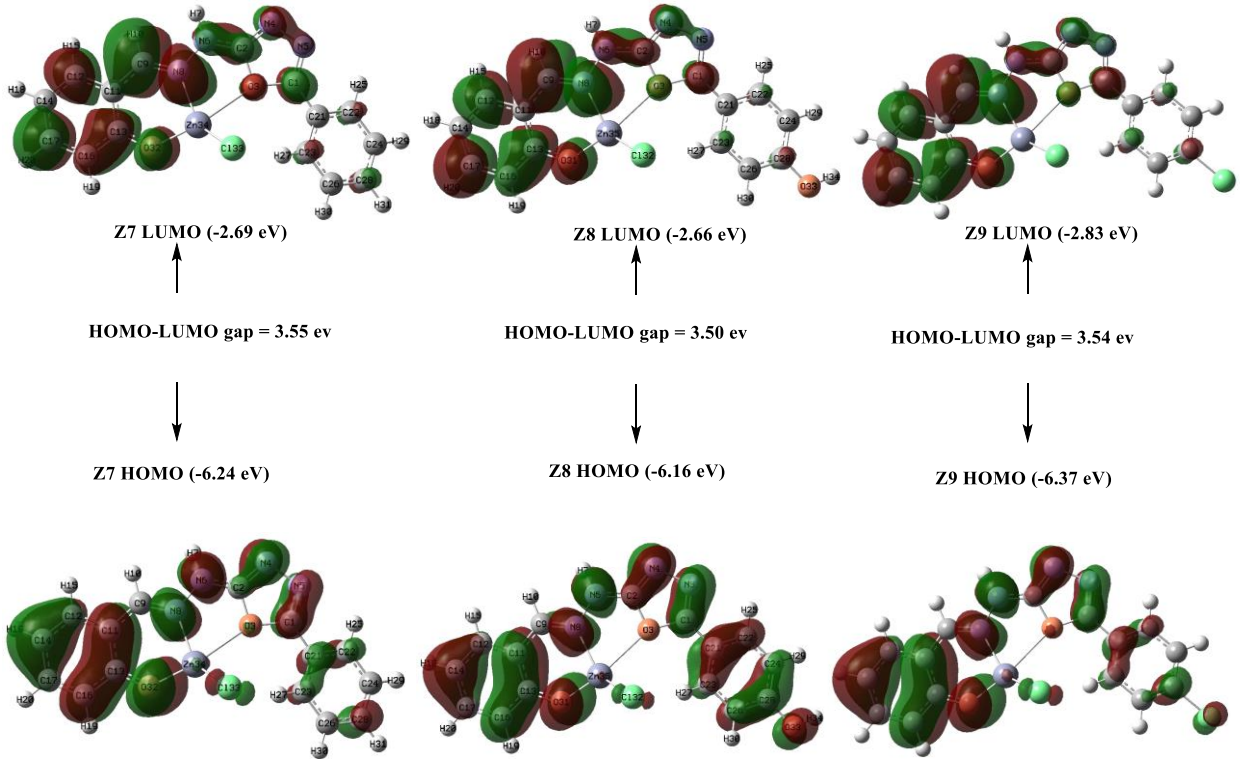

Figure 6. Energy profile of the frontier orbitals HOMO and LUMO, and HOMO-LUMO gaps for Z7, Z8, and Z9, calculated at the B3LYP functional with the 6-31+G(d,p) basis set for C, H, O, N, and Cl atoms and LANL2DZ basis set for Zn atom in DMSO as solvent.

Thermal analysis

All the complexes (Z1–Z9) appeared in an analogous decomposition style, with mass lacking in all four steps. The curves of DSC and TG for complexes Z7–Z9 appeared at the first stage; complexes offer an exothermic peak between 175 and 280 °C (obs. 34%, calc. 30%) attributed to the removal of Cl from the complex. The 2nd and 3rd stages form the ligand decomposition (350–410 °C, obs. 62.87%, calc. 60.23%) and depart from the metal atom that is then oxidized to obtain the definitive remains as a MO at 500.43–550.76 °C [42].

DNA-binding assays

Because DNA interactions were carried out in a Tris–HCl/NaCl buffer, the complexes' stability had to be tested. After 96 hours, no significant change in the absorbance or emission spectra was observed. Therefore, the lack of significant absorbance/emission changes without a significant wavelength shift predicted the stability of complexes in this buffer.

Electronic absorption titration

Electronic spectroscopy investigates the change in spectral profiles during the titration of complexes with CT–DNA. Although there was no discernible shift in the position of the intra-ligand band as CT–DNA concentrations increased, there was a strong hyperchromic effect. The complexes may interact with DNA via groove binding [43]. The presence of synergic non-covalent interactions such as external contact (electrostatic binding), hydrogen bonding, and groove surface binding (major or minor) outside the DNA helix has been linked to hyperchromic. The data for the binding constant (Kb) for complexes (Z1–Z9) is determined to be in the range of 0.85–2.82X10^3 M^{-1}, corresponding to the obtained arrangement of hyperchromic [44]. The complex Z5 appears to have the highest affinity for linking with CT–DNA. Complex linking intensities decrease in the following order: Z5 > Z4 > Z6 > Z3 > Z7 > Z8 > Z9 > Z2 > Z1. Kb data indicate that DNA was strongly bound to the complex Z5 due to the (–OH) substituent connected to the aromatic ring (Table S4) [45].

Fluorescence studies

Fluorescence titration (EB) is used to investigate the mode of interaction between the complexes (Z1-Z9) and CT–DNA (EB). The induced emission intensity at 432-445 nm was reduced when complexes were added to DNA pretreated with EB [46]. The observed quenching is due to the photoelectron transfer mechanism. These complexes bind to DNA via non-covalent groove binding modes. Therefore, the extent of the reduction in emission intensity is used to determine the relative binding of these complexes to CT–DNA. For complexes (Z1-Z9), the Stern-Volmer quenching constant value Ksv was calculated as a slope of Io/I against [DNA]/[complex] and observed to be between 0.38 and 1.76 X 10^{-2} M^{-1} (Figure 7). As a result of the findings, it was determined that Z6 has the highest Ksv values with CT–DNA. At the same time, the linking strength of the other complexes reduces in the arrangement Z5> Z4> Z6> Z2> Z1> Z3> Z8> Z7> Z9. The trend of DNA binding affinities obtained from spectral absorption studies is reflected in the binding capacity for DNA in complexes in the arrangement Cu(II)>Ni(II)>Zn(II) [46].

Properties of viscosity

Viscosity measurements on CT–DNA were performed to confirm the groove mode of binding complexes (Z1-Z9) with CT–DNA. Complexes bind to CT–DNA with a minor change in relative viscosity, demonstrating that these complexes preferentially bind to CT–DNA via minor grooves. Complexes' ability to increase the viscosity of CT-DNA varies in the following order: Z5> Z4>Z6> Z2> Z1> Z3> Z8> Z7> Z9. Z5 caused the most significant increase in DNA viscosity, indicating a better interaction with DNA, according to the findings of this study. As a result, the viscosity measurements agree with the absorption and emission results.

Studies of DNA cleavage

As shown in Figure S23, the DNA linking products show that the Cu(II) (Z4-Z6) complexes have a higher DNA linking characteristic [47]. No distinct cleavage was observed in the control, but it was observed in all the complexes. The cleavage of the complexes Z4-Z6 is visible in lanes 6–9. The variation in DNA cleavage activity was caused by the influence of substituents in complexes that interact with DNA very actively [48]. The arrangement in which DNA interacts with complexes is Z5>Z4>Z6 (Figure 2) [49]. The central metal ion may interact with the P-O bond of DNA *via* electrostatic interaction or/and Chalet linkage. As a result of the charge neutralization, a P-atom of DNA is stimulated, and one of the bonds of the P–O ester of DNA is cleaved. The results showed that the complex Z6 actively cleaves the pBR322 plasmid DNA [50].

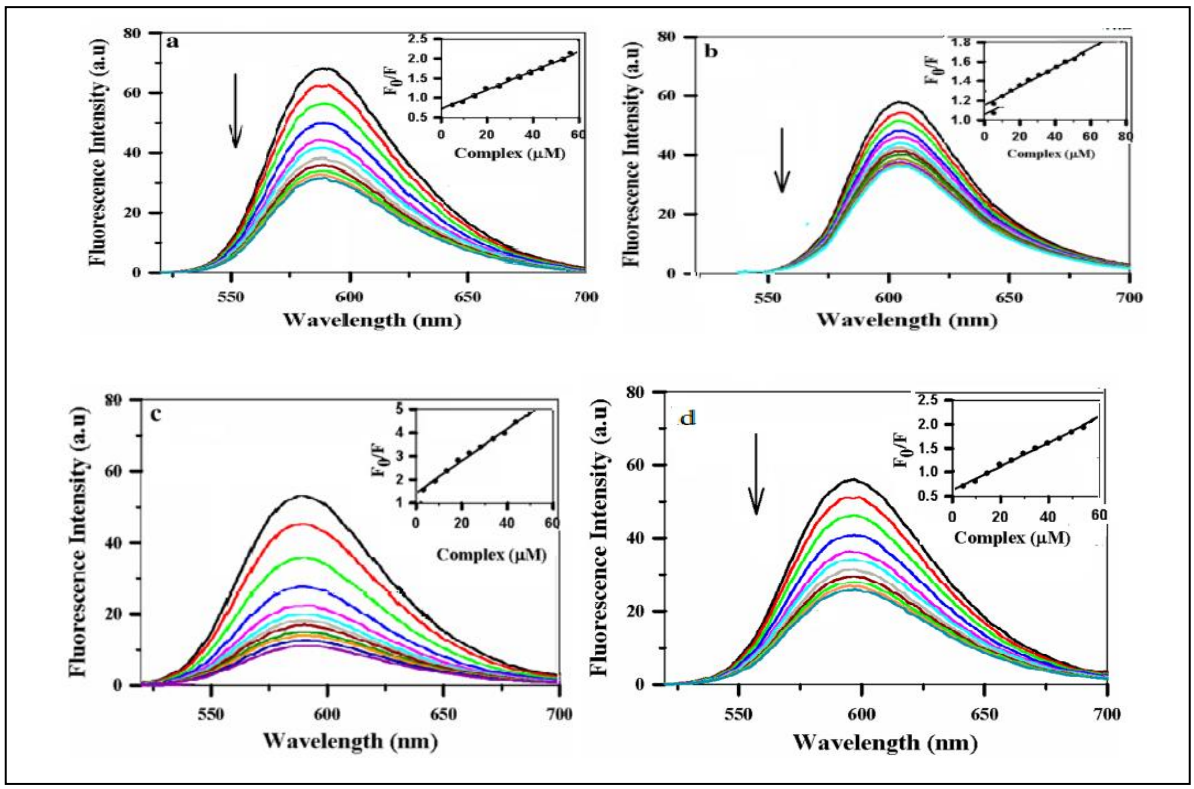

Figure 7. Fluorescence emission spectra of (50 μM) CT-DNA (2 μM) EB bound to non-attendance and existence of complexes, Z4-Z6, at diverse concentrations buffer (pH 7.9) in 10 mM Tris–HCl

Molecular docking analysis

The molecular docking analysis was used to understand the interactions of the synthesized Schiff base ligands (L1, L2, and L3) and their respective Cu^{2+} complexes (Z4, Z5, and Z6) with biotargets like DNA and protein molecules. Schiff base ligands (L1, L2, and L3) and their Cu^{2+} complexes Z4, Z5, and Z6 were docked into human DNA topoisomerase I (70 Kda) (PDB ID: 1SC7). According to the docking results, the binding energy and inhibition constant (Ki) that correspond to the interaction of Schiff base ligands (L1, L2, and L3) with 1SC7 are listed in Table S1. The interaction of the Schiff base ligands with 1SC7 is due to hydrogen bonding, pi-pi stacking (hydrophobic), and, pi-halide (hydrophobic), as shown in Figure 8. Pi-pi stacking (also known as - stacking) in chemistry refers to attractive, non-covalent interactions between aromatic rings that contain pi bonds. These interactions are important in nucleobase stacking within DNA and RNA molecules, protein folding, template-directed synthesis, materials science, and molecular recognition [51, 52]. Based on the binding energies listed in Table S1, the strongest interaction with 1SC7 was observed for the L3 ligand.

The binding energy and inhibition constant (Ki) that correspond to the interaction of Z4, Z5, and Z6 complexes with 1SC7 are listed in Table S2. The interaction of these complexes with 1SC7 is due to hydrogen bonding, pi-pi stacked (hydrophobic), pi-halide (hydrophobic), and pi-cation (electrostatic), as shown in Figure 9. Based on the binding energies listed in Table S2, the strongest interaction with 1SC7 was observed for the Z6 complex.

Cytotoxicity (in vitro) of compounds

The MTT test was used to compare complexes (Z1-Z9) versus cisplatin and two non-cancer cell lines, (PBMC) mononuclear cells of peripheral blood and (HEK) kidney of human embryonic, and three cancer cell lines, (A549) lung, (HCT-15) colon, and (HeLa), human cervical. Four various concentrations of prepared compounds (1000, 500, 250, and 100 nM) and cisplatin for 48 h were examined in triplicate, and the outcomes are evidenced by the mean ± standard perversion of two separate trials of cytotoxic [53,54]. Complexes were dissolved in DMSO, and blank specimens were taken as controls included with similar DMSO volume in experiences of cytotoxicity

to calculate solvent efficacy. IC50 concentrations were obtained from the doses that appear in studies of molecular anchorage with human topoisomerase l DNA. The presence of Cu (II) complexes (Z4-Z6) demonstrated that DNA linking is a better slope binding than other compounds, according to the results of DNA linking and molecular linking analysis [55]. IC50 concentrations were obtained from the doses that appear in studies of molecular anchorage with human topoisomerase l DNA (Table S5, Figure S24) [56, 57].

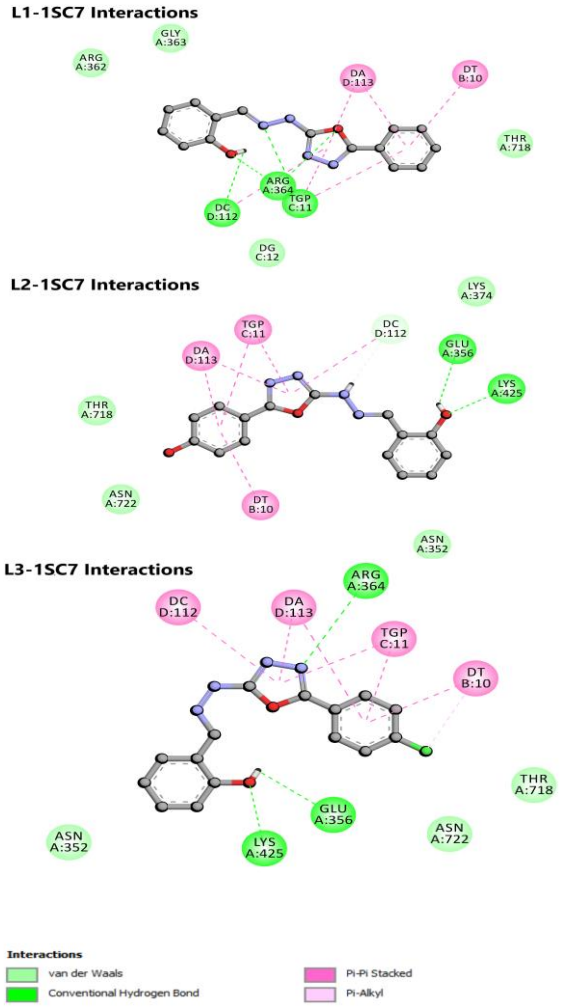

Figure 8. 2D plot of interaction between L1, L2, and L3 ligands with the human DNA topoisomerase I (70 Kda) (PDB ID: 1SC7) receptor.

CONCLUSIONS

Mononuclear Schiff base complexes of Zn (II), Cu (II), and Ni (II) have been synthesized and characterized. The complexes Z1, Z2, and Z3 adopted square planar complexes around the nickel metal ions, based on the spectral data. The Cu (II) and Zn (II) complexes (Z1, Z2, Z3, Z4, Z5, Z6, Z7, Z8, and Z9) are tetrahedral environments complexes around the central metal ions. CT– DNA appears in the groove, linking the system with all the complexes. The complex Z6 shows active cleavage of plasmid DNA from the other complexes in the absence of any external factors. The Cu(II) complexes showed greater activity in cytotoxicity than the other complexes based on the data of IC50. The cell death technique demonstrates apoptosis, but proof of the apoptosis technique is required. The strongest interaction with 1SC7 was observed for the L3 ligand and the Z6 complex according to our molecular docking results.

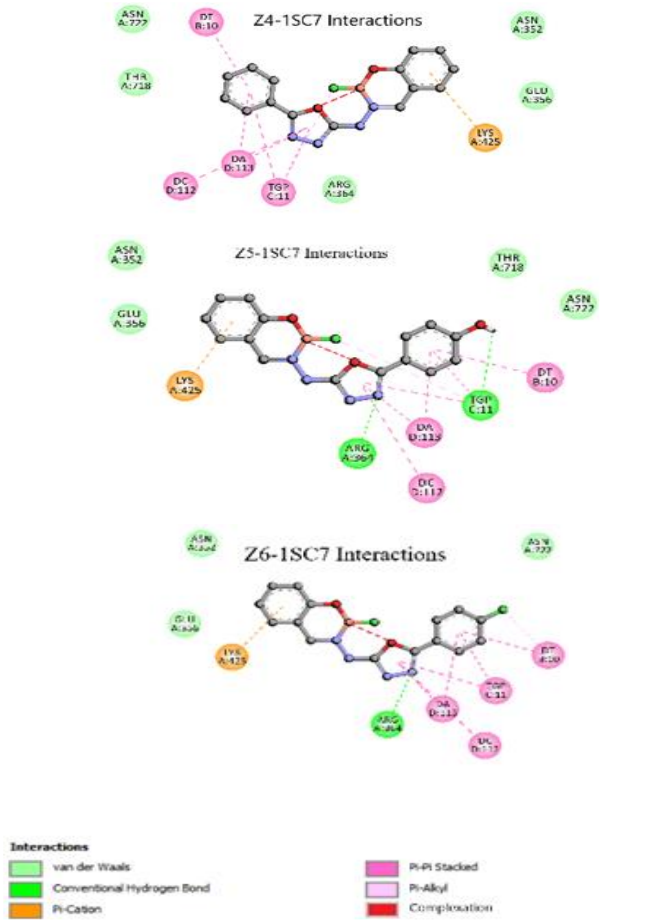

Figure 9. 2D plot of interaction between Z4, Z5, and Z6 complexes with the human DNA topoisomerase I (70 Kda) (PDB ID: 1SC7) receptor.

REFERENCES

1. Y. Nakamura, Y. Taruno, M. Sugimoto, Y. Kitamura, H.-L. Seng, S. Kong, M. Chikira, *J. Chem. Soc., Dalton Trans.*, **42**, 3745 (2013), https://doi.org/10.1039/C2DT32709

2. D. Amarante, C. Cherian, E. Megehee, *Inorganica Chim. Acta*, **461**, 239 (2472}. https://doi.org/10.1016/j.ica.2017.02.011
3. C. Rajarajeswari, L. Rangasamy, P. Mallayan, S. Eringathodi, A. Riyasdeen, M A. Akbarsha, *J. Chem. Soc., Dalton Trans.*, **42** 8347 (2013), https://doi.org/10.1039/C3DT32992E
4. Y. Nie, Z. Dai, F. Lal, G. Zhao, J. Jiang, X. Xu, M. Ying, Y. Wang, Z. Hu, H. Xu, *J. Phys. Chem. B*, **126**, 4787 (2022). https://doi.org/10.1021/acs.jpcb.2c02104
5. E. Marco, F. Gago, *Mol. Pharmacol.*, **68**. 1559 (2006), https://doi.org/10.1124/mol.105.015685
6. E. Scherbinina, D. Dar'in, P. Lobanov, *Chem. Heterocycl. Compd.*, **46**, 1109 (2010). https://doi.org/10.1007/s10593-010-0634-7
7. S.M. Basavarajaiah, B.H.M. Mramyunjayaswamy, *Indian J. Chem. B.*, **57**, 390 (2018).
8. A. Abdallah, G. Elgemeie, *Drug Des. Devel. Ther.*, 12, 1785 (2018). https://doi.org/10.2147/DDDT.S159310
9. P. Nunes, T. Pinheiro, A. Matos, I. Correia, J. Pessoa, *Ann. Med.*, **51**, 36 (2019), https://doi.org/10.1080/07853890.2018.156007*9
10. A. Haleel, P. Arthi, N.D. Reddy, V. Veena, N. Sakthivel, Y. Arun, P.T. Perumald, A.K. Rahiman, *RSC Adv.*, **4**, 60816 (2014). https://doi.org/10.1039/C4RA11197D
11. S. Voitekhovich, A. Lyakhov, L. Ivashkevich, V. Matulis, Y. Grigoriev, J. Klose, B. Kersting, O. Ivashkevich, *Z. Anorg. Allg. Chem.*, **648**, e202200213 (2022), https://doi.org/10.1002/zaac.202200213
12. W.L.F. Armarego, D.D. Perrin, Purification of Laboratory Chemicals, 4th edn., Oxford, Pergamon Press, 1996.
13. A. Haleel, D. Mahendiran, V. Veena, N. Sakthivel, A. K. Rahiman, *Mater. Sci. Eng.C*, **68**, 366 2016, https://doi.org/10.1016/j.msec.2016.05.120
14. D. Padhorny, A. Kazennov, B. Zerbe, K. Porter, B. Xia, S. Mottarella, Y. Kholodov, D. Ritchie, S. Vajda, D. Kozakov, *Proc. Natl. Acad. Sci.*, **113**, E4286 (2016), https://doi.org/10.1073/pnas.1603929113
15. L. Zeng, Y.-M. Ren, C. Cai, *ChemInform Abstract*, **43** (2012), https://doi.org/10.1002/chin.201218186.
16. S. Betanzos-Lara, C. Gómez-Ruiz, L.R. Barrón-Sosa, I. Gracia-Mora, M. Flores-Álamo, N. Barba-Behrens, *J. Inorg. Biochem.*, **114**, 82 (2012), https://doi.org/10.1016/j.jinorgbio.2012.05.001
17. , M. Sobiesiak, T. Muziol, M. Rozalski, U. Krajewska, E. Budzisz, *New J. Chem.*, **38**, 5349 (2014), https://doi.org/10.1039/C4NJ00977K
18. A.B.P. Lever, Inorganic Electronic Spectroscopy, 2nd edn., Elsevier, Amsterdam, 1984, p. 18.
19. B. Naskar, R. Modak, D.K. Maiti, S.K. Mandal, J.K. Biswas, T.K. Mondal, S. Goswami, *Polyhedron*, **117**, 834 (2016), https://doi.org/10.1016/J.POLY.2016.07.018
20. J. Ravichandran, P. Gurumoorthy, C. Karthick, A. K. Rahiman, *J. Mol. Struct.*, 1062, 147 (2014), https://doi.org/10.1016/j.molstruc.2014.01.026
21. M. J. Frisch et al., *Gaussian*, Inc., Wallingford CT, 2009.
22. E. A. Al-Razaq, N. Buttrus, W. Al-Kattan, A.A. Jbarah, M. Almatarneh, *J. Sulfur Chem.*, **32**, 159 (2011), https://doi.org/10.1080/17415993.2010.550617
23. T. Tüğsüz, F. Sevin, *J. Mol. Struct. Theochem.*, **775**, 29 (2006), https://doi.org/10.1016/j.theochem.2006.07.004
24. M. Zhang, Y. Wang, X. Wang, B. Zhao, W. Ruan, *J. Phys. Chem. C*, **125**, 17125 (2021), https://doi.org/10.1021/acs.jpcc.1c02058
25. M.K. Assefa, J.L. Devera, A.D. Brathwaite, J.D. Mosley, M.A. Duncan, *Chem. Phys. Lett.*, **640**, 175 (2015), https://doi.org/10.1016/j.cplett.2015.10.031
26. J. Tölle, M. Böckers, J. Neugebauer, *J. Chem. Phys.*, **150**, 181101 (2019), https://doi.org/10.1063/1.5097124
27. M. Cossi, N. Rega, G. Scalmani, V. Barone, *J. Comput. Chem.*, **24**, 669 (2003).
28. A. Peraza, V. Sojo, F. Ruette, M. Sánchez, , A. Eleonora, *J. Comput. Methods Sci. Eng.*, **12**, 397 (2012), https://doi.org/10.3233/JCM-2012-0428.
29. P. A. Ravindranath, S. Forli, D. Goodsell, A. Olson, M. Sanner, *Comput. Biol.*, **11**, e1004586 (2015), https://doi.org/10.1371/journal.pcbi.1004586.
30. BIOVIA, Dassault Systèmes, Discovery studio 4.0 client, 21.1.00, San Diego, Dassault Systèmes, 2021.
31. F.R. Dollish, W.G. Fateley, F.F. Bentley, Characteristic Raman Frequencies of Organic Compounds, Wiley, 1974.
32. D. Lin-Vien, N.B. Colthup, W.G. Fateley, J.G. Grasselli, The Handbook of Infrared and Raman Characteristic Frequencies of Organic Molecules, Academic Press. San Diego, 199l.
33. G. Socrates, Infrared and Raman Characteristic Group Frequencies: Tables and Charts, NewYork, Wiley, 1980.
34. A.L. Baskerville, M. Targema, H. Cox, *R. Soc. Open Sci.*, **9**, 211333 (2022), https://doi.org/10.1098/rsos.211333
35. T. Culpitt, K. Brorsen, M. Pak, S. Hammes-Schiffer, *J. Chem. Phys.*, **145**, 044106 (2016), https://doi.org/10.1063/1.4958952
36. A. Becke, *J. Chem. Phys.*, **150**, 241101 (2019) ,https://doi.org/10.1063/1.5109675.
37. V. Saheb, F. Rezaei, S. Hosseini, *Comput. Theor. Chem.*, 1051, **123** (2014), https://doi.org/10.1016/j.comptc.2014.10.027
38. M. Mosquera, *Phys. Rev. A.*, **88**, 022515 (2013), https://doi.org/10.1103/PhysRevA.88.022515.
39. K. Pernal, *J. Chem. Phys.*,**136**, 184105 (2012), https://doi.org/10.1063/1.4712019

40. R. Al-Shemary, B. Zaidan, N. Al-marsomy, *Diyala Journal for Pure Science*, **13**, 21 (2017), https://doi.org/10.24237/djps.1303.189C
41. R. Friedman, E. Ahlstrand, K. Hermansson, *J. Phys. Chem. A.*, **121**., 2643 (2017), https://doi.org/10.1021/acs.jpca.6b12969
42. S. Al-Ashqar, *Open J. Inorg. Chem.*, **6** 195 (2016), https://doi.org/10.4236/ojic.2016.63015
43. P. Deepika, H.M. Vinusha, M. Begum, R. Ramu, P. Shirahatti, M.N.N. Prasad, *Heliyon*, **8**, e09648. (2022), https://doi.org/10.1016/j.heliyon.2022.e09648
44. D. Moon, S. Jeon, M. Mazúr, M. Valko, J.-H. Choi, *J. Mol. Struct.*, 1231, 129897 (2021), https://doi.org/10.1016/j.molstruc.2021.129897
45. M. Manjunath, A. Kulkarni, G. Bagihalli, S. Malladi, S. Patil, *J. Mol. Struct.*, **1127**, 314 (2016), https://doi.org/10.1016/j.molstruc.2016.07.123
46. B. Lombardi, R. Brown, C. Gendy, C. Chang, T. Chivers, R. Roesler, *Organometallics*, **36**, 3250 (2017), https://doi.org/10.1021/acs.organomet.7b00396
47. S. Kou, K. Zhou, Z. Lin, Y. Lou, J. Shi, Y. Liu, *J. Mol. Liq.*, **328**, 115491 (2021), https://doi.org/10.1016/j.molliq.2021.115491
48. X. Chen, B. Wang, K. Zhou, Y. Lou, S. Kou, Z. Lin, J. Shi, *ChemistrySelect*, **4**, 3774 (2019), https://doi.org/10.1002/slct.201900089
49. F. Shahri, A. Niazi, A. Akrami, *Iranian Journal of Mathematical Chemistry*, **7**, 47 (2016), https://doi.org/10.22052/IJMC.2016.11869
50. D.M. Suresh, D. Sajan, Y.-P. Diao, I. Nemec, I.H. Joe, V. Jothy, *Spectrochim. Acta A Mol.*, **110**, 157 (2013), https://doi.org/10*.1016/j.saa.2013.01.067
51. N. Tidjani-Rahmouni, N.H. Bensiradj, S. Djebbar, O.\ Benali-Baitich, *J. Mol. Struct.*, **1075**, 254 (2014), https://doi.org/10.1016/j.molstruc.2014.06.067
52. A. Gubendran, G.G.V. Kumar, M.P. Kesavan, G. Rajagopal, P. Athappan, J. Rajesh, *Appl. Organomet. Chem.*, **32**, e4128 (2018), https://doi.org/10.1002/aoc.4128
53. C.R. Martinez, B.L. Iverson, *Chem. Sci.*, **3**, 2191 (2012), https://doi.org/10.1039/C2SC20045G
54. A. Campo, E. Cabaleiro-Lago, J. Carrazana-García, J. Rodriguez-Otero, *J. Comput. Chem.*, **35**, 1290 (2014), https://doi.org/10.1002/jcc.23623.
55. H.H. Alkam, W.M. Alwan, R.K.R. Alshemary, *Int. J. Pharm. Res.*, **14**, 3370 (2021), https://doi.org/10.31838/ijpr/2021.13.01.429
56. N.M. Majeed, S.A. Al-Sahab, R.K. Al-Shemary, *Int. J. Pharm. Res.*, **13**, (2021), https://doi.org/10.31838/ijpr/2021.13.01.428
57. E.M. Mohammed, R.K R. Al-Shemary, *Int. J. Pharm. Res.*, **13**, (2021), https://doi.org/10.31838/ijpr/2021.13.01.427